*Microsc. Microanal. Microstruct.* **6** (1995) 587–599 OCTOBER/DECEMBER **1995**, PAGE 587

Classification
*Physics Abstracts*
61.16Bg — 68.35Dv — 82.65Yh

# Local Chemistry at Interfaces and Boundaries: Ceramic and Electronic Composite Materials

R.W. Carpenter([1,*]), J.S. Bow([1]), M.J. Kim([1]), K. Das Chowdhury([1]) and W. Braue([2])

([1]) Center for Solid State Science and the Science and Engineering of Materials Program, Arizona State University, Tempe AZ 85287-1704, U.S.A.
([2]) German Aerospace Research Establishment (DLR), Materials Research Institute, 51147 Cologne, Germany

*(Received June 20; accepted June 28, 1995)*

**Abstract.** — The spatial extent of chemical solute distributions that formed in interfaces between platinum or silicon nitride and silicon carbide or in silicon nitride grain boundaries during high temperature processing of these composites has been investigated by position resolved nanospectroscopy, Z-contrast imaging and energy selected imaging. The solute distributions resulted from intentional sintering aid additions or interfacial reaction. The distribution widths normal to the nominal interface/boundary planes, called chemical interface/boundary widths, were much larger than the corresponding structural widths of the same boundaries and interfaces, determined by HREM imaging. Qualitative agreement between the three methods used to determine chemical widths was excellent. Differences in count rate resulting from beam current differences among the methods resulted is some predictable quantitative disagreements in absolute chemical widths. Energy selected imaging proved to be a very fast, efficient method for examination of chemical distributions over large specimen areas.

## 1. Introduction

The mechanical and electrical properties of composites depend markedly on the composition of their internal interfaces and boundary regions, which, in turn, are strongly dependent on the synthesis techniques used for these materials [1, 2]. Impurity or other concentration gradients at interfaces or boundaries in ceramic and electronic materials are expected to be of smaller spatial extent than in the case of most metals, where they have often been observed, because solute element solubilities and phase field widths are both generally smaller than for metal systems. Nevertheless energy of mixing considerations lead to the expectation that gradients will exist, however small, when sufficient mobility exists, and that the gradients should be detectable by high spatial resolution analytical methods [1].

In this paper we report applications of electron energy loss and energy dispersive X-ray nanospectroscopy and Z-contrast and energy selected TEM imaging to detection of solute distributions (chemical widths) at grain boundaries and interfaces in platinum/silicon carbide and silicon nitride/silicon carbide whisker composites.

(*) also with the Chemical, Bio and Materials Engineering Department.

Light elements such as oxygen, nitrogen and carbon are very important constituents of the composites examined and they were our primary concern. For this reason small probe electron energy loss spectroscopy is an obvious direct analytical method for detection of elemental distributions at interfaces and grain boundaries, with complementary small probe X-ray spectroscopy. Spectroscopic spatial resolution is limited by probe size/current density and electromechanical stability; it is also a very slow point by point process when gradients are examined, therefore parallel recorded energy selected imaging was also used to examine some ceramic grain boundaries and interfaces. Z-contrast STEM imaging was explored as a simpler alternative to X-ray point spectra for mapping for heavy metal distributions in ceramic grain boundaries and energy selected imaging was used to examine lighter elemental distributions.

## 2. Instrumentation and Specimen Materials

**2.1** INSTRUMENTATION — Elemental distributions at interfaces and grain boundaries in edge-on orientation were examined using a Philips field emission 400 TEM with super twin objective lens; a standard Gatan 666 parallel energy loss spectrometer was used for EELS. Focused probe current distributions for this microscope have been determined [3] for nanospectroscopy and were used with a computer based control system [4] for stepping the probe across the microstructural features of interest with spectrum acquisition and storage at each step, to obtain position resolved electron energy loss spectroscopy (PREELS). Focused probe optics permit a wide choice of probe sizes, depending on the current desired, which largely determines the acquisition time at each step. We used a 3 nm diameter probe for most of the results shown here, which required 100 ms collection time at each step. The probe current density was about $10^4$ amp/cm$^2$. Appropriate core edge peaks were background stripped, integrated, and the resulting net intensities plotted *vs.* specimen position coordinate normal to edge-on interfaces/boundaries, to produce elemental distribution plots. The same optics and control system were used for EDXS with either an EDAX or Link spectrometer.

A Zeiss 912 omega filter microscope was used at 120 keV for energy selected imaging. Core loss images for Al, O, Si, N and C were recorded at 31,500 X with a CCD camera, using exposure times up to 30 s. The incident current density at the specimen in this microscope has been reported to be 5 amp/cm$^2$ [5]. Energy selected images (ESTEMI) were background stripped by subtracting a preedge image multiplied by a constant less than unity so that the intensity of each background stripped energy selected image was everywhere positive. A VG HB501 STEM was used for Z-contrast imaging, at 100 keV. Inner collection angles ranged from 70 to 100 mrad. It is fitted with a Link windowless EDXS spectrometer. An ISI 002B(200KeV) was used for HREM images. The Scherzer resolution of this microscope is 0.18 nm.

**2.2** SPECIMEN MATERIALS — Elemental distributions in high purity Pt/SiC and conventionally processed $Si_3N_4$/SiC whisker reinforced ceramic matrix composites are described here. The Pt/SiC interfaces were made by deposition of Pt thin films on vicinal single crystal Si-terminated (0001) $\alpha$ 6H-SiC substrates. The single crystals were produced by Cree Research and the depositions and subsequent heat treatments were performed at North Carolina State University. Pt metal was deposited onto the unheated substrates by thermal evaporation in a UHV chamber at room temperature. All post deposition heat treatments were also performed in UHV. Details of deposition and annealing were described elsewhere [16]. The ceramic matrix composite specimen was synthesized at the German Aerospace Research Laboratory (DLR) in Cologne from $\alpha$ - $Si_3N_4$ powder containing 20 wt.% Huber or American Matrix SiC whiskers, with 5.5 wt.% $Y_2O_3$ plus 1.1. wt.% $Al_2O_3$ sintering aids added. The powder mixture was cold pressed and then presintered

for 1 h at 1500 °C in 0.1 MPa argon. Complete densification was achieved by hot isostatic pressing at 1780 °C in 190 MPa argon for 1 h [6].

The interfaces/boundaries in these specimens represent two extremes for electronic and ceramic materials. The initial state for Pt/SiC, after room temperature deposition, was an interface that was atomically sharp, both chemically and structurally. Only slight traces of oxygen, but no other impurities, were detectable in some lateral positions along the interface by PREELS, and there was not sufficient mobility for any mixing by diffusion during deposition. Only during post deposition heat treatment was atomic mobility sufficient to permit mixing and interface reaction, as shown below. The addition of oxide sintering aids to the non-oxide ceramic matrix composite, on the other hand, can be viewed as "impurity" addition early in the high temperature processing cycle. The sintering aids are a well-known addition whose purpose is to form a liquid in the particle compact interstices during processing, so that densification can proceed by liquid phase transport because solid state diffusion is very slow in the covalent non-oxide ceramics. The question of interest for the ceramic matrix composites is whether elemental gradients in the $Si_3N_4$ or SiC crystals bounding the regions containing liquid sintering aid can form by solid state diffusion of sintering aid constituents into the $Si_3N_4$ and SiC and out diffusion of constituents of these crystals into the sintering aid liquid regions, during processing. Chemically sharp interfaces/boundaries may not exist in this composite because all processing occurred at high temperature, despite the sharp appearance of HREM interface images.

## 3. Results and Discussion

### 3.1 NANOSPECTROSCOPY

**3.1.1** Pt/SiC *Interfaces* — For annealing temperatures up to 650 °C there was no detectable general new phase formation at the Pt/SiC interface. After 20 min annealing at 650 °C position resolved X-ray analysis normal to the edge-on interface revealed a small amount of diffusion of Pt into the SiC as shown in Figure 1. The ~ 6 nm chemical width of the interface is a result of convolution of the initially sharp interface with the 3 nm diameter incident focused probe. Probe

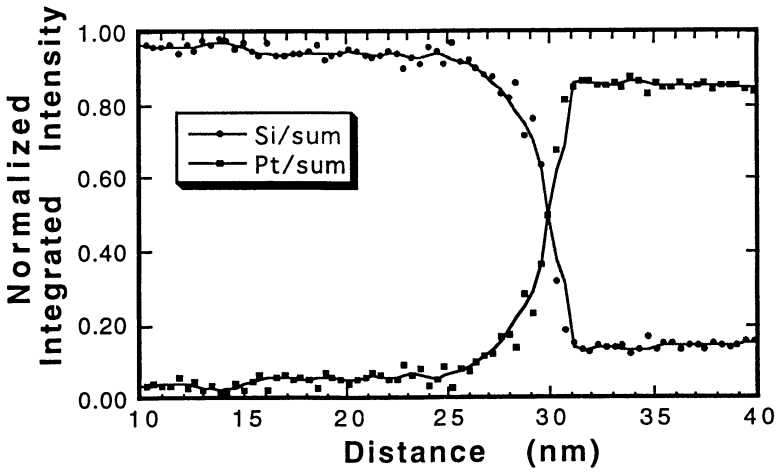


Fig. 1. — EDX compositional profiles of Si and Pt of 650 °C/20 min annealed Pt/6H-SiC. Each data point is the net integrated peak intensity for the element of interest, Si or Pt, normalized by the sum of the net integrated Si and Pt intensities at the same position relative to the interface.

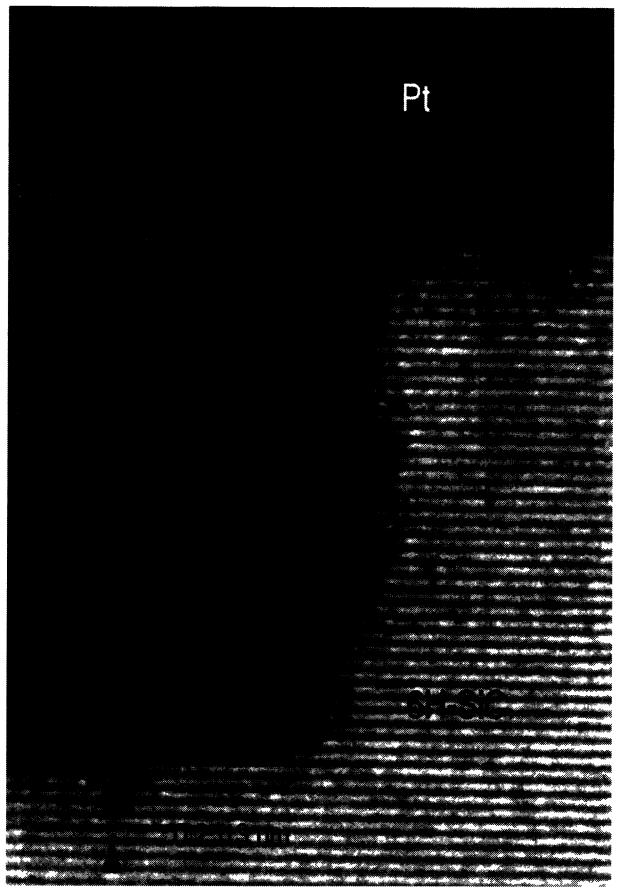


Fig. 2. — Two beam HREM image shows a large interface step, 650 °C/20 min annealed Pt/6H-SiC. The penetrated region (local reaction zone) shows dark contrast similar to the Pt layer.

diameter-current distribution relations for the microscope used (Phillips 400 FEG) reported earlier [3] showed that an ~ 6 nm experimental chemical width corresponded to an atomically sharp $Si/SiO_x$ chemical interface scanned by a 3 nm incident focused probe [17]. The smooth curvature of the Pt and Si distributions on the SiC side of the interface shown in Figure 1 indicate that a small amount of Pt and Si interdiffusion in the SiC occurred. HREM showed that a few isolated local reaction zones had penetrated *into* the SiC at the interface. One example is shown in Figure 2. The reaction zone lattice spacing was 0.229 nm, determined from lattice fringe profile analysis, which is smaller than the SiC (0001) spacing, which is 0.251 nm, but close to Pt(111) with spacing 0.226 nm, indicating that the reaction zone was a Pt(Si,C) solid solution. After 20 min anneal at 750 °C an extensive interfacial reaction zone formed, as shown in Figure 3. The reaction zone can be divided into three discontinuous sublayers nominally parallel to the substrate plane, labeled A, B and C. Diffraction analysis showed that A was nominally $Pt_2Si$, B was an amorphous phase and C was the Pt(Si,C) solution containing inclusions of the amorphous phase. PREELS and X-ray spectroscopic analysis across the reaction zone showed that the elemental gradients existed at all sublayer interfaces. The A layer structure corresponded to $Pt_2Si$, for example, but regions near the substrate were Si-rich and those near the C layer were Pt rich. The B layer was primarily

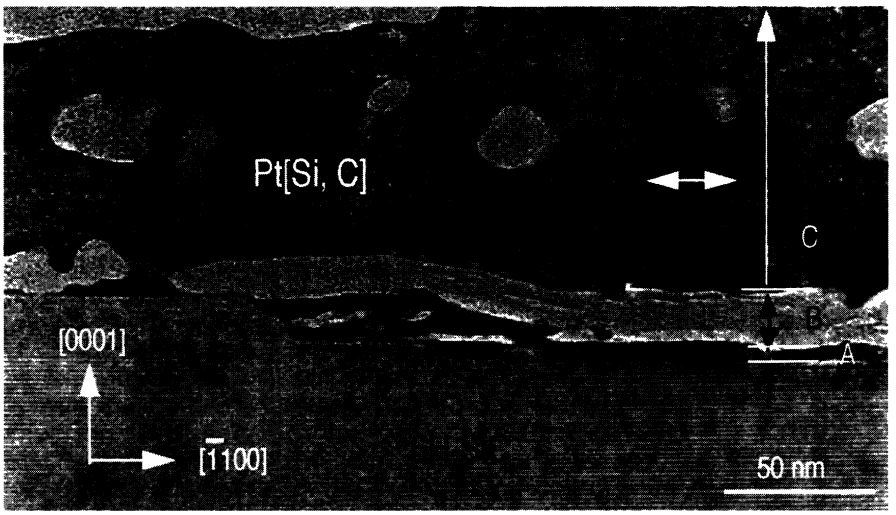


Fig. 3. — XTEM micrograph of 750 °C/20 min annealed Pt/6H-SiC. The reaction zone is divided into three sublayers, labeled A,B, and C. See text for discussion.

amorphous carbon and the C layer matrix was face centered cubic solution containing inclusions of the B layer amorphous material. The B layer, however, was not simply amorphous carbon. It was markedly susceptible to electron beam damage unlike common amorphous carbon specimens, and was thinned more rapidly then the other reaction zone layers during ion beam specimen preparation, complicating elemental analysis. Details of its structure and composition are still being investigated.

**3.1.2** $Si_3N_4$/SiC(w) *Composites* — Position resolved EELS measurements of oxygen gradients that formed during synthesis at whisker/matrix interface are shown in Figures 4 and 5. These two figures, which come from two different locations along the same interface, show that the lateral interface oxygen distribution is discontinuous and that the oxygen distribution width, called the *chemical* interface width, is appreciably larger than the *structural* width of the interface visible in the HREM images. Similar PREELS experiments were performed on matrix grain boundaries in these composites. Large oxygen chemical widths were again observed, as shown in Figure 6, but with an important difference: the oxygen distributions across matrix grain boundaries were laterally continuous along the boundaries. Structural widths of both interfaces and grain boundaries in these ceramic composites were variable from about 2 nm to vanishing by small widths, as shown in Figure 6. Vanishingly small structural widths in HREM images (cf Fig. 6) were not a reliable indicator of the presence or absence of oxygen enrichment or nitrogen depletion. Where measurable chemical widths occurred, i.e. positive or negative distribution peaks, they were 10 to 120 times wider than the corresponding structural widths. Substitution of oxygen for nitrogen in the silicon nitride and carbide crystals comprising the composite implied that aluminum and possibly yttrium also substituted for some silicon in the bounding crystals, to maintain electrical neutrality.

**3.2** Z-CONTRAST IMAGING OF Y-DISTRIBUTION IN CERAMICS — Substitution of Si for Al in $\beta$-$Si_3N_4$ when oxygen substitutes for nitrogen results in the formation of $\beta'$-SiAlON, with an

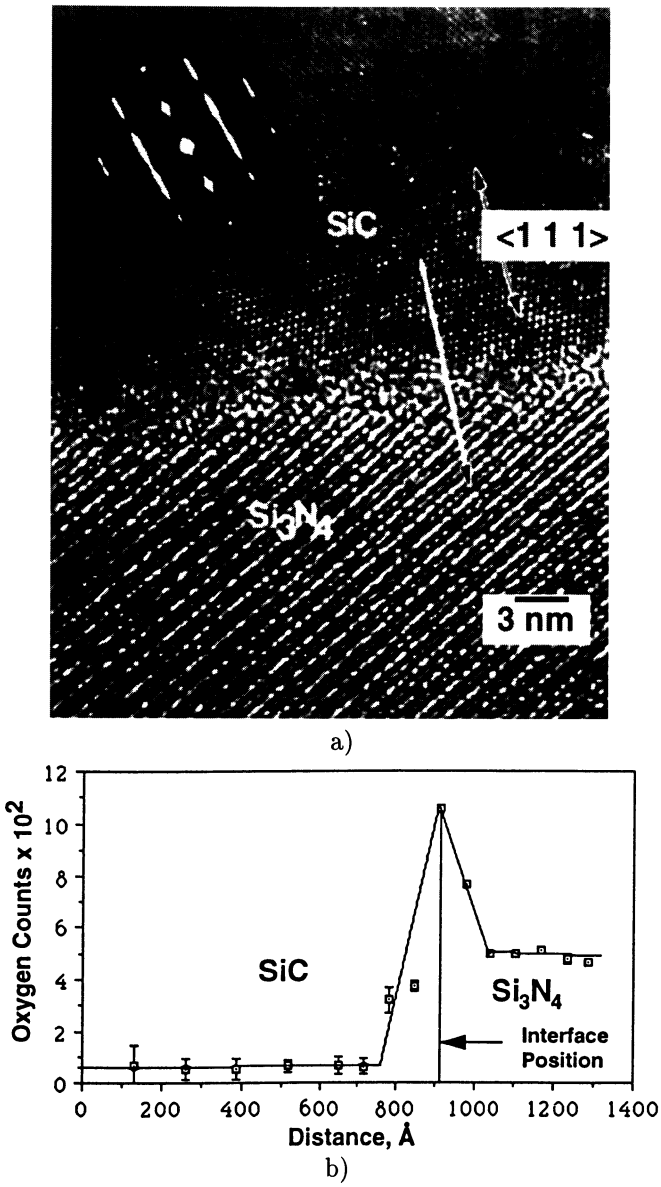


Fig. 4. — a) HREM image of an SiC(w)/$Si_3N_4$ interface. Structural width of this interface was approximately 1.5 nm. SiC is in < 110 > zone axis orientation. $Si_3N_4$ is oriented for $g$ = < 002 > two beam diffraction. The arrow crossing the interface indicates the focused probe scan path for PREELS. b) Variation of oxygen content across the SiC/$Si_3N_4$ interface of Figure 4a, along the scan path indicated by the arrow. Note the high oxygen content in the interface region. The chemical interface width, defined by the oxygen peak width, is about 28 nm.

expansion of the solid solution lattice resulting from the difference in ion radii [8]. Yttrium has been observed earlier in $\alpha'$-SiAlON sqlutions based on the $\alpha$-$Si_3N_4$ polymorph, but solution of Y in $\beta$-$Si_3N_4$ has not been observed, so its distribution in the present specimens is of particular interest [9].

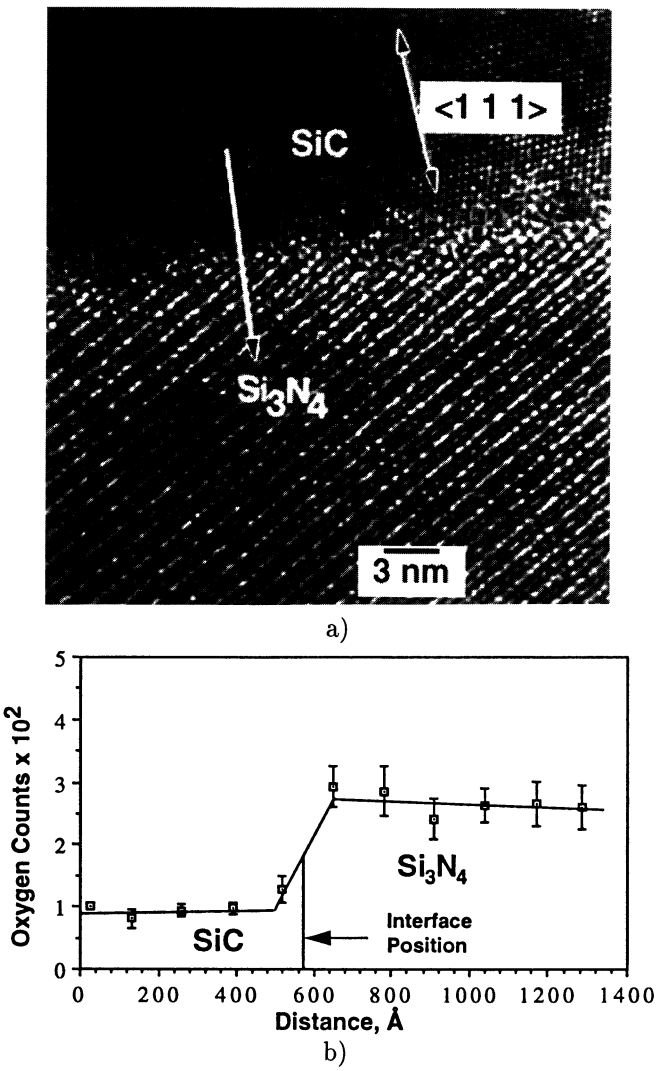


Fig. 5. — a) HREM image of a portion of the same interface show in Figure 4a. This region is about 20 nm away from the region show in Figure 4a. The structural width of this region is about 1.1 nm. The orientation of the SiC(w) and $Si_3N_4$ crystals bounding the interface are as in Figure 4a; the arrow crossing the interface marks the probe scan path for the nanospectroscopy results shown in Figure 5b. b) Variation of the interfacial region oxygen content for the region shown in Figure 5a. For this region no preferential high oxygen content was observed, but a difference in background oxygen content for the two bounding crystals was evident. The chemical width was about 15 nm in this region.

The atomic number of Y, 39, is appreciably higher than the atomic number of all the other ceramic composite constituents, whose average atomic number was about 10. This large difference implied that Z-contrast would be a very useful although non-spectroscopic method for imaging the Y distribution at interfaces/boundaries, with X-ray spectroscopy used to confirm that observed contrast resulted from Y, and also to confirm the expected Al distribution which would not produce appreciable Z-contrast. These methods avoid interference expected to occur during electron

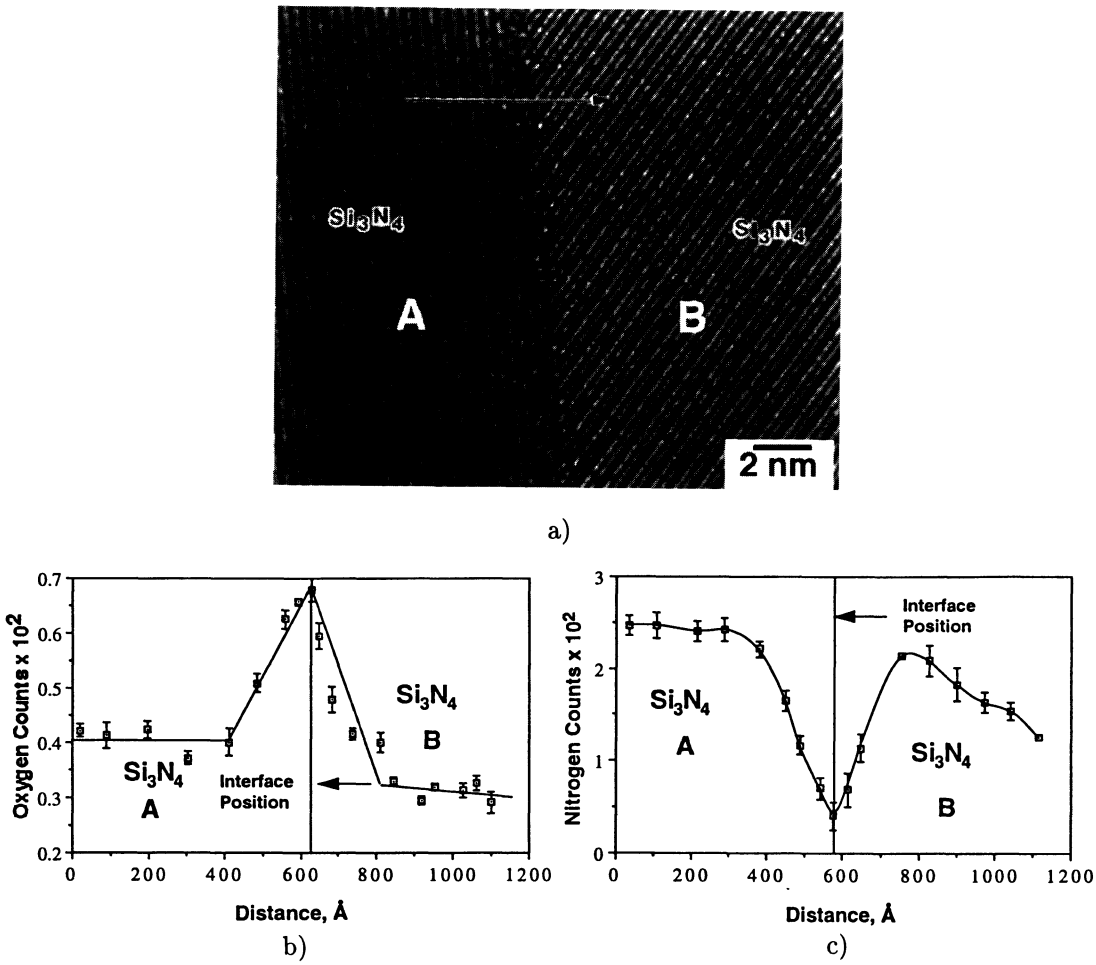


Fig. 6. — a) An HREM image of an edge-on matrix grain boundary in a Huber SiC(w) composite. The width of the disordered region at the boundary, i.e. the structural width, is about 0.3 nm. Scan path is marked by the arrow. Grains A and B are oriented for $g = < 110 >$ and $< 100 >$ two beam diffraction. b) Variation in oxygen content with distance from the boundary for the scan path shown in Figure 6a. The chemical width of this oxygen distribution was about 41 nm. c) Variation of nitrogen content with distance from the boundary, for the scan path shown in Figure 6a. The chemical width of this nitrogen distribution at the interface was about 45 nm.

energy loss spectroscopy between broad Y-M and carbon and nitrogen K peaks, and Y- N and Si nitride, carbide and oxide low loss peaks [10].

A VG HB 501 STEM was used for the Z contrast imaging. When the inner collection angle of the annular dark field detector is increased to large angles (> 70 mrad) these images can be interpreted as two dimensional chemical maps for high atomic number constituents, provided that local thickness variations are avoided and channeling effects are suppressed by proper selection of diffracting conditions [11, 12]. Some of these results are shown in Figure 7. The oblique amplitude modulated Z-contrast image (Fig. 7a) indicates that Y is distributed continuously along matrix grain boundaries in the $Si_3N_4$/SiC (w) composite of interest. A line scan through this image (Fig. 7b) viewed along the boundary indicated that the Y distribution was symmetric about the plane of the boundary. The specific presence of Y within the structural width of the boundary

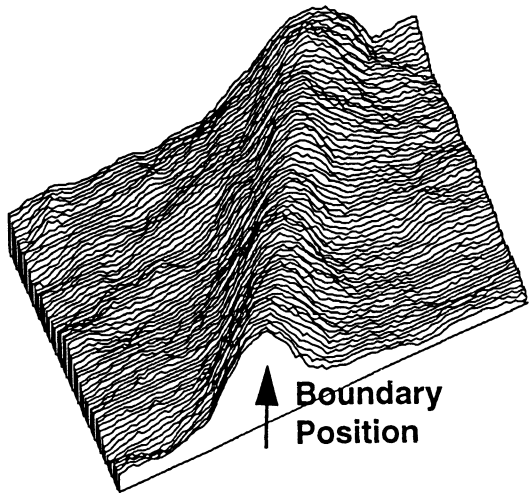


a)

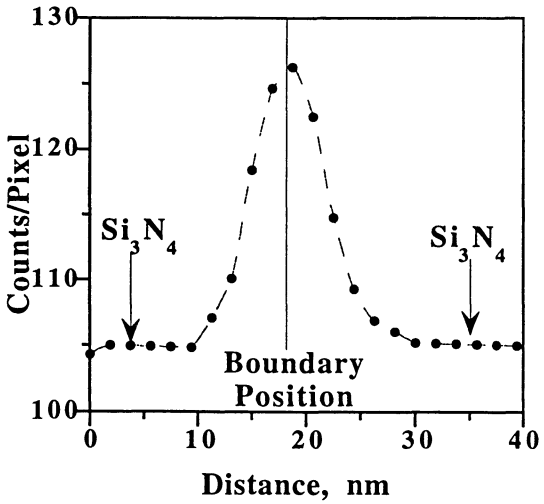


b)

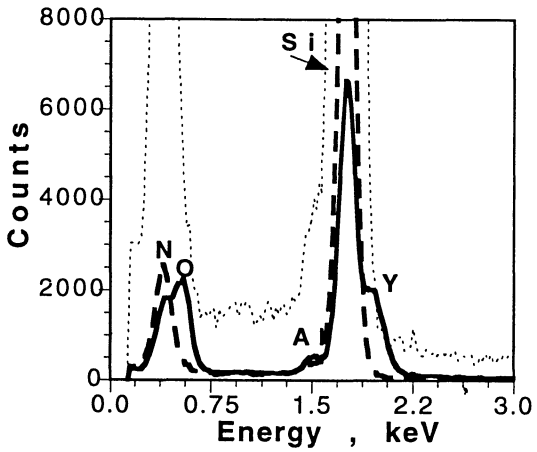


c)

Fig. 7. — a) Oblique view of amplitude-modulated Z-contrast image of a matrix grain boundary in edge-on orientation. The yttrium distribution is laterally continuous along the boundary and there is no evidence for differential ion thinning at this particular boundary. b) Z-contrast image intensity line scan across an edge-on matrix grain boundary in the Huber composite. The intensity is proportional to yttrium content. The boundary is a mirror plane for the yttrium distribution curve. Other solutes are present, as shown in Figure 7c. c) Windowless X-ray spectra at points in the plane of the grain boundary corresponding to Figure 7b (solid curve) and displaced 14 nm away from the boundary plane into one of the bounding crystals (dashed curve). The latter spectrum is also shown amplified by 10× (narrow dotted curve). The asymmetric shoulders on the Si peak in the amplified spectrum show that O, Y and Al are present in the matrix 14 nm away from the boundary plane. Note that more Al than Y was present in the matrix, the converse of these element contents in the plane of the boundary.

and at lower concentration 14 nm away from the boundary "plane" in one of the bounding crystals was established by the EDXS results shown in Figure 7c. The EDXS results also showed that the Al and O distributions followed the Y distributions, and that the O and N distributions correlated well with the PREELS results shown in Figure 6. Additional Z-contrast and EDXS experiments confirmed that the Y and Al distributions in SiC(w)/$Si_3N_4$ interfaces contained the same lateral discontinuities observed for oxygen distributions shown in Figures 4 and 5. The Z-contrast technique proved to be very useful for investigating Y distributions, and is expected to be as useful for other materials systems that contain high Z elements, e.g. Pt/Si C. Spectroscopic confirmation of Z- contrast results is required, however, because the technique is indirect. Its primary advantages are simplicity, sensitivity in appropriate materials systems and the potential for near atomic resolution.

**3.3** ENERGY SELECTED TEM IMAGING (ESTEMI) — Energy selected imaging using an omega ($\Omega$) filter on the Zeiss 912 microscope with slow scan CCD camera acquisition is a parallel image collection process potentially capable of providing the same chemical distribution information for boundaries/interfaces as described above, but in image mode. Figure 8 shows bright field and ESTEMI images for a matrix grain boundary in the $Si_3N_4$ matrix/SiC(w) composite of the same kind for which PREELS results were given above. A grain boundary connecting two triple junctions (at upper left and lower right of the image) is shown. The edge of the foil is at upper right of the image. It can be seen that the results are in excellent qualitative agreement with the earlier PREELS results. The ESTEMI show that the grain boundary and triple junctions are Al-rich, Si depleted, O-rich, N-depleted and the triple junctions but not the grain boundary appear to be C-rich, in Figures 8b through f, respectively. The contrast in Figure 8f was attributed to carbon, but Y in the triple junctions may also have contributed to this image contrast, so this particular result requires further investigation. The white box shown in Figure 8a defines a strip 50 pixels in lateral width along the edge-on boundary. Intensity along this strip was background stripped and summed to obtain the intensity plots shown below each image. Single pixel wide intensity plots were generally too noisy to be useful. The irradiation half-angle for the energy selected images were 2.5 mrad, with an exposure time of up to 30 s. The numbers on each of the plots are image widths. The bright field image (Fig. 8a) indicates that the nominal structural width of this grain boundary was $\sim$ 3.8 nm; the small maxima at each edge of the boundary are Fresnel fringes, indicating that the image was recorded slightly out of focus. The chemical widths of the boundary ranged from 9.2 to 6.2 nm, except for Figure 8f, which was so noisy even for the 50 pixel width sum that a chemical width could not be defined. The detectable chemical widths were all greater than the structural width, in excellent qualitative agreement with PREELS results. However both the absolute values of the chemical widths and the ratios of chemical to structural widths are smaller for ESTEMI than the corresponding values obtained using PREELS and HREM. Two contributions to this difference are apparent. The most accurate method for measurement of structural width is HREM. Diffraction contrast or Fresnel imaging methods typically produce diffuse images of boundaries/interfaces at very high magnification and wide images at lower magnification. The effect of Fresnel fringing on images of the boundaries/interfaces of interest here can be complex. We showed earlier that Fresnel fringes can result from a difference in mean inner potential at the interface/boundary region because a composition difference generally exists between the thin so-called amorphous phase and the bounding crystals, or they can result in the image from a chemically clean boundary simply because a difference in scatterer density (atom density) generally exists between the plane of the boundary and the bounding perfect crystals, or from grooves at the intersections of the boundary/interface plane with the specimen surfaces caused by TEM specimen thinning technique [13]. The presence of the fringes will usually result in a reduction of the apparent chemical to structural width ratio relative to the same ratio calculated

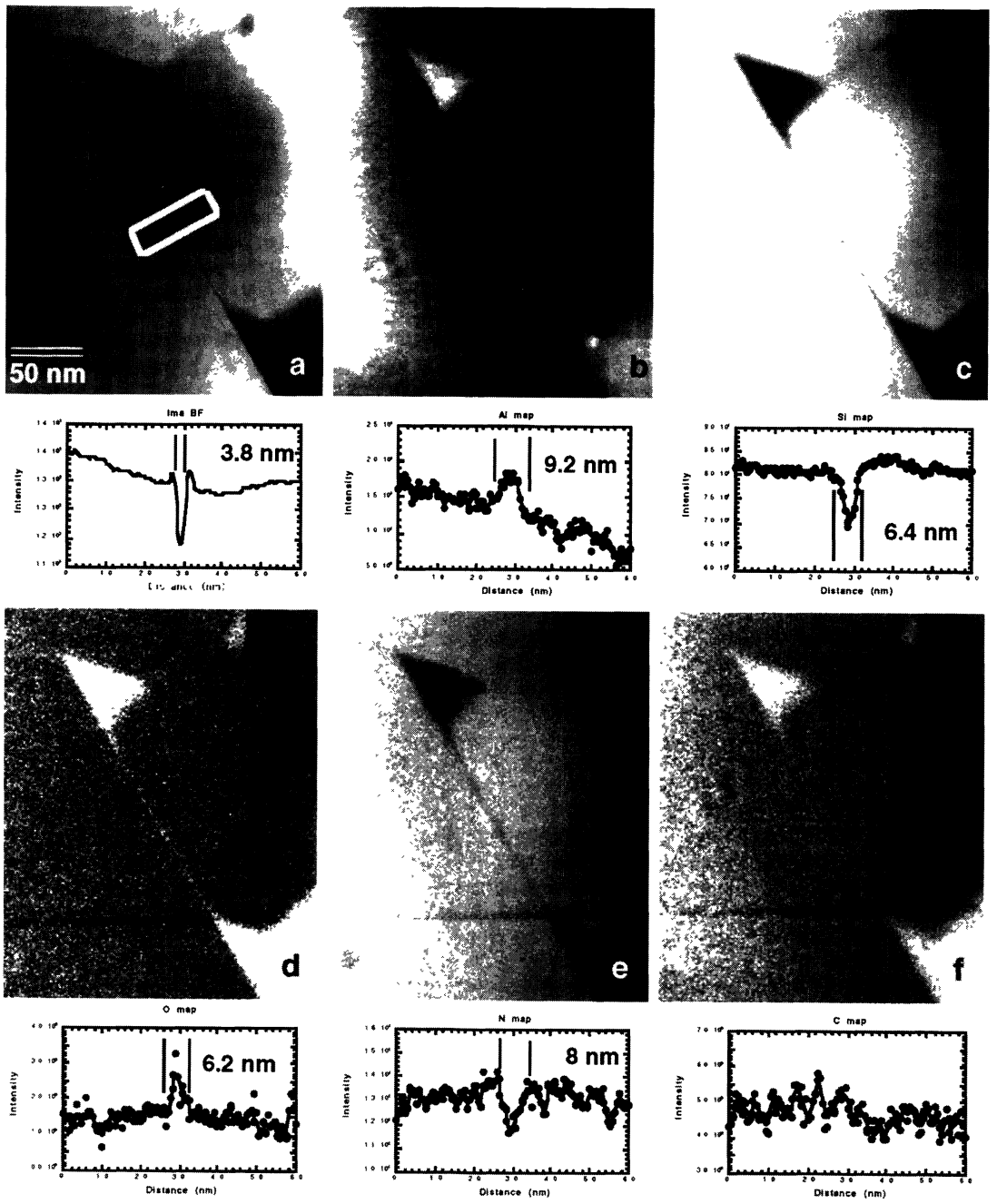


Fig. 8. — Bright field and energy selected images of an edge-on grain boundary. (a) Bright field; (b) Al-L, energy window (EW) = [80, 100], 10 s collection time (CT); (c) Si-L, EW = [120, 140], 10 s CT; (d) O-K, EW = [545, 565], 30 s CT; (e) N-K, EW = [425, 445], 30 s CT; (f) C-K, EW = [300,320], 20 s CT.

using an HREM structural image width. To use the HREM width the microscope used for ESTEMI must have resolution capability necessary for HREM, or the HREM structural width must be determined at the same position along the boundary/interface in a separate microscope. The point resolution of the Zeiss microscope used for the present work is $\sim 0.35$ nm, so we used the bright field diffraction contrast boundary image width (Fig. 5a) to calculate the ratio; we have not yet measured the HREM structural width of this particular boundary in a separate microscope, but we expect such a measurement to result in width ratios larger than the present value of $\sim 1.5$ to 2.5. Our chemical widths determined by ESTEMI for three boundaries ranged from $\sim 4$ to 28 nm, which are approximately two-thirds the range of the widths determined by PREELS. The minimum detectable solute mass fraction (MMF) for electron energy loss and characteristic X-ray spectroscopies is proportional to $(J\tau)^{-1/2}$, where $J$ is the incident flux and $\tau$ is the spectrum acquisition time [14, 15]. As noted above, the field emission probe current density we used for PREELS was about $10^4$ amps/cm$^2$, and incident current density for the Zeiss 912 was reported to be about 5 amps/cm$^2$ [5]. The sensitivity of the field emission PREELS technique, then, is $\sim 50$ times larger than energy selected imaging assuming other experimental variables are equal, or, alternatively, an energy selected image would require about 200 s collection time for elemental detection sensitivity equal to a 100 ms PREELS collection time, but such extended collection times did not prove to be practical. The difference in sensitivity resulted in truncation of the ESTEMI elemental distributions at long distances from the boundaries, producing narrower chemical widths that the PREELS method widths.

## 4. Summary and Conclusions

Position resolved electron energy loss and characteristic X-ray spectroscopies were used at a spatial resolution of about 3 nm to show that solute element gradients will occur at Pt/SiC interfaces and at matrix grain boundaries and reinforcement/matrix interfaces in silicon carbide whisker reinforced/silicon nitride matrix ceramic composites. An analytical electron microscope with a high brightness field source is necessary for these experiments. Z-contrast STEM imaging (also called high angle annular STEM dark field imaging) proved useful for examining heavy element distribution (Yttrium) in the ceramic matrix composite. This technique should be readily applicable to other appropriate material systems and come into widespread use. We used energy selected imaging for the first time to examine the same ceramic matrix composite boundary/interface elemental distributions. The ESTEMI results were in excellent qualitative agreement with our nanospectroscopy results. Quantitative agreement can be improved by using HREM images for structural width measurements when chemical/structural width ratios are of interest, and absolute chemical width measurements can be brought into closer agreement by using larger total beam current for energy selected imaging. Because ESTEMI is a parallel imaging technique and the incident current is distributed over the imaged area, *total* probe current is the important variable here, not current density in a small focused probe. Thermionic sources with relatively large emitting area are more likely to produce improvements in this technique than field emission sources. The technique is much faster than pointwise small probe nanospectroscopy and has much to recommend it, especially for examination of elemental distributions over large specimen areas.

Our results show unequivocally that nonequilibrium solute distribution gradients can be expected near interphase interfaces and grain boundaries in refractory covalently bonded materials. In general the chemical widths of these distributions will be larger than the commonly observed HREM structural widths of these boundaries/interfaces. High spatial resolution field emission source analytical methods are required to detect these distributions, because they are smaller ($<$ 3 to tens of nanometers) than comparable nonequilibrium solute distributions that may extend for several hundred nanometers in metallic alloys where atomic mobilities and solid

solubilities are usually both large [18]. The discontinuities in lateral solute distributions observed in the ceramic matrix composite whisker/matrix interfaces, but not in the matrix grain boundaries of these composites, result from near atomic scale surface facets on the SiC whiskers. Several research groups have shown that SiC whisker surfaces are faceted by sets of nonparallel {111} planes resulting from rotation twins formed during whisker growth [19, 20]. The surface projections formed by intersections of the nonparallel {111} planes extend above the whisker surfaces to form direct crystal to crystal contacts at discontinuous locations with adjacent silicon nitride crystals, resulting in laterally discontinuous sintering aid and therefore chemical width distributions. The unusual solution of yttrium into the $\beta$-$Si_3N_4$ matrix crystals only occurs in the presence of $Al_2O_3$. Loehman and Rowcliffe [21] showed by X-ray diffraction methods that when small amounts of $Al_2O_3$ and $Y_2O_3$ were heated with $\beta$-$Si_3N_4$ the resulting lattice expansion was larger than occurred for $Al_2O_3$ solution alone in the nitride, but that no expansion occurred when only $Y_2O_3$ and $\beta$-$Si_3N_4$ were heated, indicating that the presence of $Al_2O_3$ is required for dissolution of $Y_2O_3$ in $\beta$-$Si_3N_4$. Our nanospectroscopy results confirm Loehman and Rowcliffe's conclusion, which was based on indirect diffraction evidence.

**Acknowledgements**

The research was supported by the United States Department of Energy, Basic Energy Sciences, Division of Materials Sciences under grant DE-FG02-45510 (Dr. Otto Buck).

**References**

[1] M. Ruhle, A. G. Evans, M. F. Ashby and J. P. Hirth Eds., Metal-Ceramic Interfaces, Acta-Scripta Metallurgica Proc. Series, vol. 4 (Pergamon Press, New York, 1990).
[2] Pozzi G. *et al.*, Proc. ATTI, del XVII Congresso di Microscopia Eletrronica, SiME, Lecce (1989).
[3] Weiss J. K., Carpenter R.W. and Higgs A.A., *Ultramicros.* **36** (1991) 319.
[4] Weiss J.K., Rez P. and Higgs A.A., *Ultramicros.* **41** (1992) 291.
[5] Berger A., Mayer J. and Kohl H., *Ultramicros.* **55** (1994) 101.
[6] Das Chowdhury K., Carpenter R.W., Braue W., Liu J. and Ma H., *J. Am. Ceram. Soc.* **78** (1995) 2579.
[7] Angelini P., Mader W. and Becher P.F., *Mater. Res. Soc. Symp. Proc.* **78** (1987) 241 (Mater. Res. Soc., Pittsburgh, PA, USA).
[8] Jack K.H., Progress in Nitrogen Ceramics, F.L. Riley Ed. (Martinus Nijhoff Publishers, The Hague, 1983) pp. 45-60.
[9] Ekstroem T. and Mygren M., *J. Am. Ceram. Soc.* **75** (1992) 259.
[10] Skiff W.M., Carpenter R.W. and Lin S.H., *J. Appl. Phys.* **64** (1988) 6328.
[11] Pennycook S.J., Berger S.D. and Culbertson R.G., *J. Micros.* **155** (1986) 229.
[12] Liu J. and Cowley J.M., *Ultramicros.* **34** (1990) 119.
[13] Das Chowdhury K., Carpenter R.W. and Kim M.J., Microscopy: The Key Research Tool, *Special Publication of the Microscopy Society of America* **22** (1992) 61.
[14] Joy D. and Maher D.M., in Scanning Electron Microscopy 1977/I, O. Johari Ed. (IIT Resch. Inst. Chicago, 1977) p. 325.
[15] Issaacson M. and Johnson D., *Ultramicros.* **1** (1975) 33.
[16] Porter L.M., Glass R.C., Davis R.F., Bow J.S., Kim M.J. and Carpenter R.W., *Mater. Res. Soc. Symp. Proc.* **282** (1993) 471.
[17] Catalano M., Kim M.J., Carpenter R.W., Das Chowdhury K. and Wong J., *J. Mater. Res.* **18** (1993) 2893.
[18] Nutt S.R. and Carpenter R.W., *Mater. Sci Engr.* **75** (1985) 169.
[19] Wang L., Wada H. and Allard L.F., *J. Mater. Res.* **7** (1992) 148.
[20] Nutt S.R., *J. Amer. Ceram Soc.* **71** (1988) 149.
[21] Loehman R.E. and Rowcliffe D.J., *J. Amer. Ceram. Soc.* **63** (1980) 144.